

Targeting the activity of T cells by membrane surface redox regulation for cancer theranostics

Received: 1 October 2021

Accepted: 12 October 2022

Published online: 19 December 2022

 Check for updates

Changrong Shi^{1,8}, Qianyu Zhang^{1,8}, Yuying Yao², Fantian Zeng¹, Chao Du¹, Sureya Nijati¹, Xuejun Wen¹, Xinyi Zhang¹, Hongzhang Yang¹, Haoting Chen², Zhide Guo¹, Xianzhong Zhang¹, Jinhao Gao³, Weisheng Guo²✉, Xiaoyuan Chen^{4,5,6,7}✉ & Zijian Zhou¹✉

T cells play a determining role in the immunomodulation and prognostic evaluation of cancer treatments relying on immune activation. While specific biomarkers determine the population and distribution of T cells in tumours, the in situ activity of T cells is less studied. Here we designed T-cell-targeting fusogenic liposomes to regulate and quantify the activity of T cells by exploiting their surface redox status as a chemical target. The T-cell-targeting fusogenic liposomes equipped with 2,2,6,6-tetramethylpiperidine (TEMP) groups neutralize reactive oxygen species protecting T cells from oxidation-induced loss of activity. Meanwhile, the production of paramagnetic 2,2,6,6-tetramethylpiperidine 1-oxyl (TEMPO) radicals allows magnetic resonance imaging quantification of the T cell activity. In multiple mouse models, the T-cell-targeting fusogenic liposomes led to efficient tumour inhibition and to early prediction of radiotherapy outcomes. This study uses a chemical targeting strategy to measure the in situ activity of T cells for cancer theranostics and may provide further understanding on engineering T cells for cancer treatment.

The efficacy of immune-activation-related cancer therapy greatly relies on the performance of tumour-infiltrating T cells¹. The past decades have witnessed substantial progress in engineering T cells for cancer treatments, such as chimeric antigen receptor T cell immunotherapy

and T-cell-receptor-engineered T cell therapy^{2,3}. Unfortunately, the broad effectiveness of T-cell-based cancer therapy in the clinic is still elusive⁴. One major caveat is that the immunosuppressive tumour microenvironment may pose great challenge to T cells in terms of

¹State Key Laboratory of Molecular Vaccinology and Molecular Diagnostics & Center for Molecular Imaging and Translational Medicine, Department of Laboratory Medicine, School of Public Health, Xiamen University, Xiamen, China. ²Department of Minimally Invasive Interventional Radiology, State Key Laboratory of Respiratory Disease, School of Biomedical Engineering & the Second Affiliated Hospital, Guangzhou Medical University, Guangzhou, China. ³State Key Laboratory of Physical Chemistry of Solid Surfaces & The Key Laboratory for Chemical Biology of Fujian Province, Department of Chemical Biology, College of Chemistry and Chemical Engineering, Xiamen University, Xiamen, China. ⁴Departments of Diagnostic Radiology, Chemical and Biomolecular Engineering, and Biomedical Engineering, Yong Loo Lin School of Medicine and College of Design and Engineering, National University of Singapore, Singapore, Singapore. ⁵Clinical Imaging Research Centre, Centre for Translational Medicine, Yong Loo Lin School of Medicine, National University of Singapore, Singapore, Singapore. ⁶Nanomedicine Translational Research Program, NUS Center for Nanomedicine, Yong Loo Lin School of Medicine, National University of Singapore, Singapore, Singapore. ⁷Institute of Molecular and Cell Biology, Agency for Science, Technology, and Research (A*STAR), Singapore, Singapore. ⁸These authors contributed equally: Changrong Shi, Qianyu Zhang. ✉e-mail: tjuguoweisheng@126.com; chen.shawn@nus.edu.sg; zhouz@xmu.edu.cn

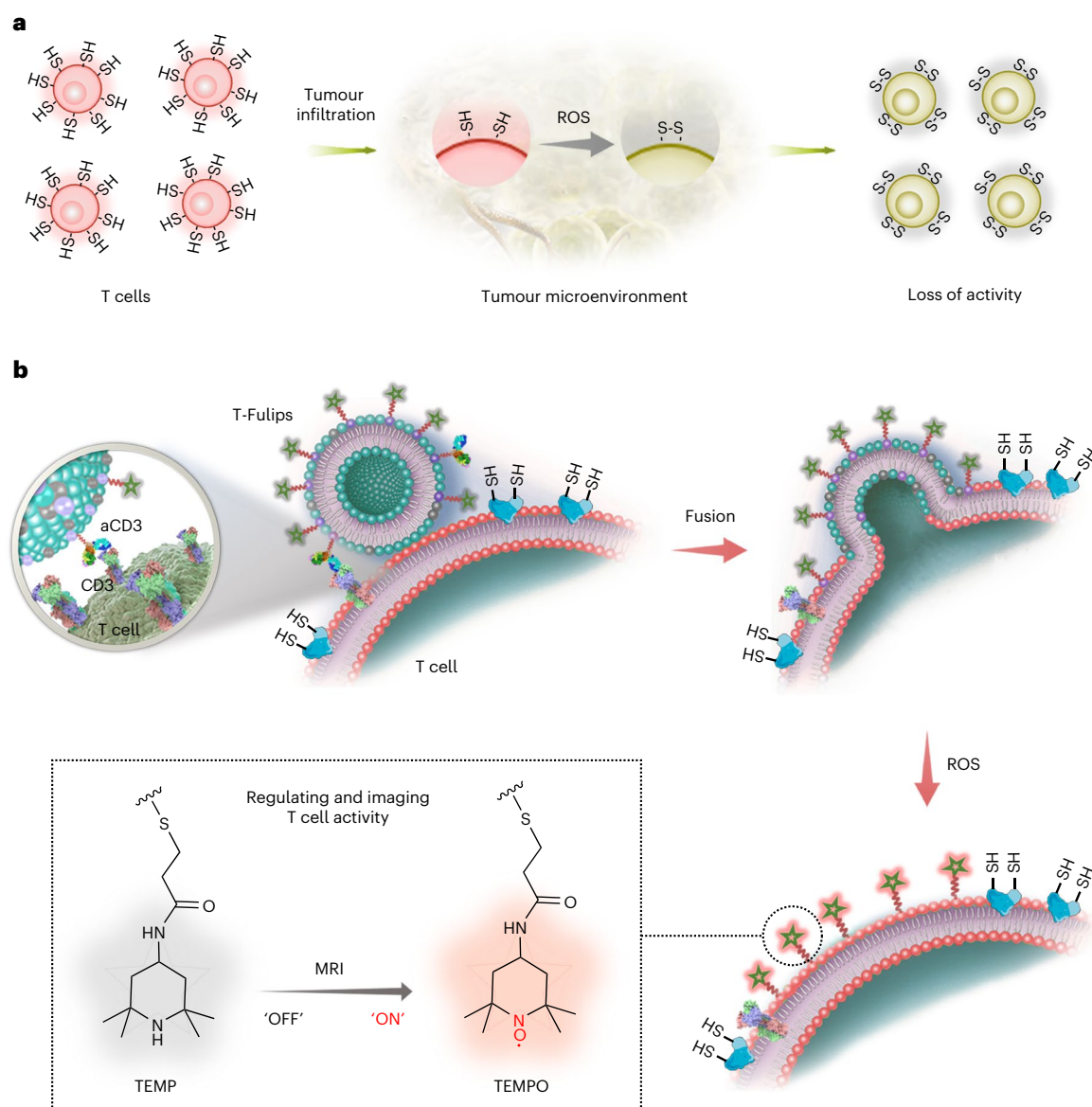


Fig. 1 | Targeting the activity of T cells by exploiting the -SH and S-S balance on the membrane surface of the T cells. **a**, Schematic illustration of the phenomenon that tumour-infiltrating T cells may lose their activity in the tumour microenvironment due to the ROS-induced oxidation of -SH groups into S-S groups on the membrane surface of the T cells. **b**, The surface redox status of T cells could be a vivid target for regulating and imaging the activity of T cells by

well-designed T-Fulips. The T-Fulips serve as ROS 'decoys' harbouring T cells from oxidation-induced loss of activity. Meanwhile, this process turns the diamagnetic TEMP into paramagnetic TEMPO radicals, which provides prominent changes of the proton T_1 relaxation time in a '0 to 1' manner for activated MRI quantification of the activity of T cells.

the survival, proliferation and cytotoxic activity when they reach the tumour region⁵. Moreover, tumour heterogeneity further complicates this situation as evidenced by the fact that a combined rate of patients with responses to immunotherapy is as low as 30% or less in the clinic⁶. Therefore, assessing the status of T cells in tumours is essential to the immunomodulation and prognostic evaluation of cancer immunotherapy⁷. Although the traditional biopsy method is considered the golden standard, its invasiveness and lack of accuracy necessitate pursuing alternatives. To this end, molecular imaging approaches that noninvasively and anatomically assess T cells *in vivo* have gained much momentum⁸. Current strategies targeting the specific biomarkers of T cells have been widely exploited to reveal the population and distribution of T cells in tumours⁹. However, recent studies have indicated that only 10% or less of tumour-infiltrating CD8⁺ T cells were active to recognize and kill tumour cells in ovarian and colorectal cancer,

whereas T cell infiltration has been serving as a major prognostic marker in clinics^{10–12}. Therefore, insight into the *in situ* immune activity of T cells in tumours is appealing for the better immunomodulation and prognosis of cancer treatment. However, molecular imaging approaches to delineate the *in situ* immune activity of T cells in tumours remain a formidable challenge.

The tumour microenvironment is composed of not only tumour cells, immune cells and the extracellular matrix, but also the physiological environment such as the pH, growth factors and reactive oxygen species (ROS) present, and so on¹³. Recent progress on cancer theranostics has experienced a paradigm shift from directly targeting tumour cells towards cooperating with the physiological conditions of the tumour microenvironment (for example, pH and ROS)^{14,15}. Given the cytotoxicity of ROS in directly killing cancer cells, promoting ROS generation in tumours has been widely considered for cancer

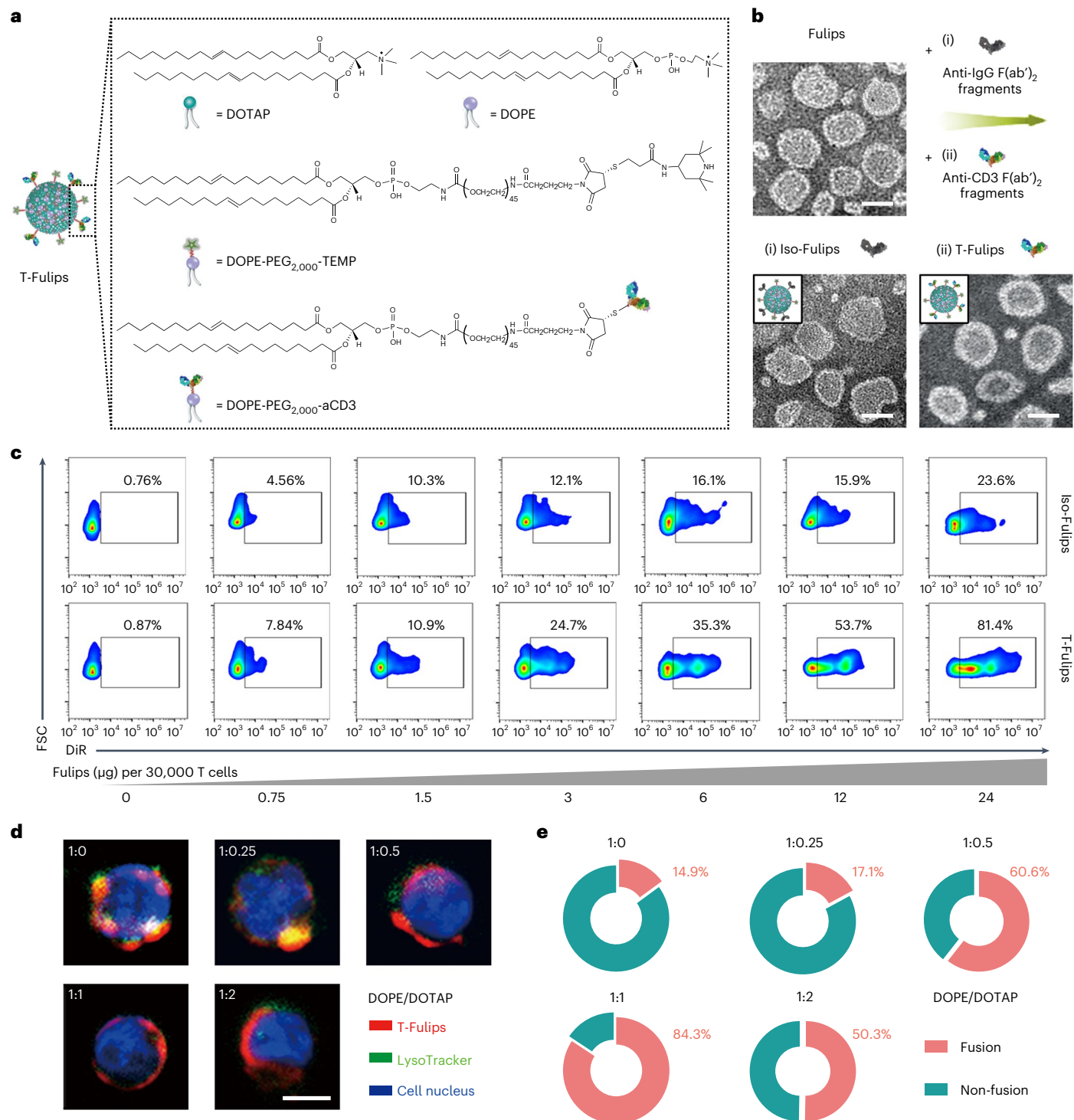


Fig. 2 | Characterizations of fusogenic liposomes. **a**, Schemes showing the composition and structural formula of various Fulips, including DOTAP, DOPE, DOPE-PEG₂₀₀₀-TEMP and DOPE-PEG₂₀₀₀-aCD3. The image at the left shows their position on the T cell. **b**, Transmission electron microscopy images of different liposomes, including Fulips (unmodified), Iso-Fulips (isotype control) and T-Fulips (T-cell-targeting anti-CD3 (aCD3) modification). The insets show the T cells. Scale bars, 50 nm. **c**, The internalization of T-Fulips and Iso-Fulips (both loaded with DiR) analysed by flow cytometry. DiR, 1,1'-dioctadecyl-3,3,3',3'-tetramethylindotricarbocyanine iodide. FSC, forward scatter measurement.

d, Confocal microscopy images showing the fusion features of the T-Fulips containing different ratios of DOPE/DOTAP incubated with murine T cells. Scale bar, 10 μm. **e**, Quantification of the fusion efficiency of the T-Fulips containing different ratios of DOPE/DOTAP incubated with murine T cells. The fusion efficiency (%F) was studied by a fluorescence resonance energy transfer assay and calculated from the fluorescence of NBD at 535 nm (F_{NBD}) as follows: $\%F = (F_{\text{NBD}} - F_0) / (F_{100} - F_0)$. The initial fluorescence of the labeled liposome suspension was recorded as 0% fluorescence (F_0) and the 100% fluorescence (F_{100}) was determined after adding Triton X-100 at 0.1% (v/v).

therapy^{14,16,17}. However, there is a pitfall in that overwhelming the ROS level in the tumour will also threaten the survival and function of immune cells, which are critical to longitudinally suppress the

tumour growth through systemic immune responses¹⁸. For instance, the surface redox status of T cells is crucial to the activity of T cells, yet is susceptible to the ROS-induced oxidation stress in the tumour

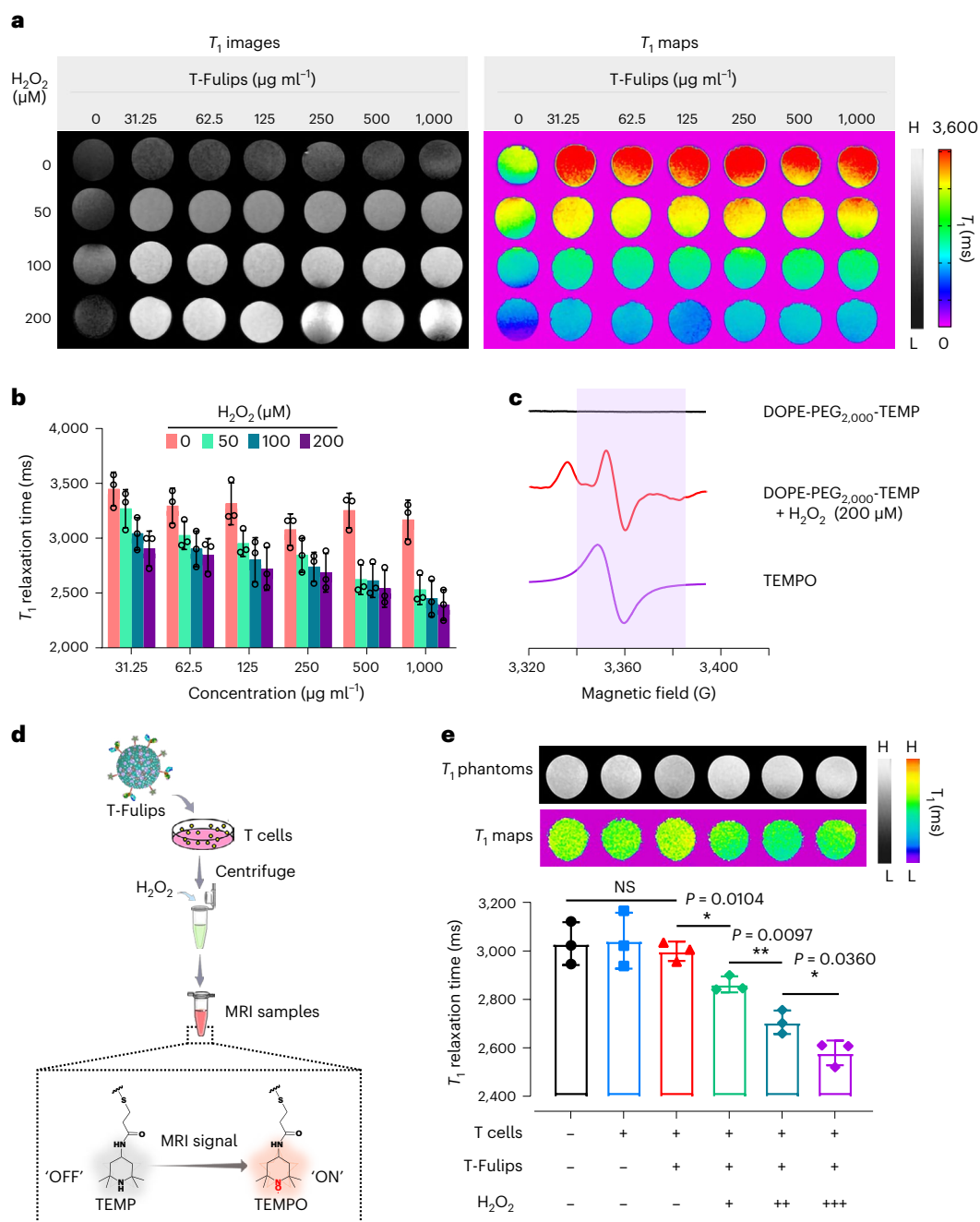


Fig. 3 | MRI measurements of T-Fulips. **a**, T₁ phantom images (left) and T₁ maps (right) of T-Fulips under different conditions. Scale bars are shown for phantoms and maps from left to right, respectively. H, high. L, low. **b**, Columns show the T₁ relaxation times of the T-Fulips under different conditions. Data are representative from three independent samples and are shown as the mean ± s.d. **c**, The electron paramagnetic resonance measurements indicate the formation of paramagnetic TEMPO radicals for the DOPE-PEG₂₀₀₀-TEMP molecules in the presence of H₂O₂. The light purple background shows the fraction of TEMPO

signals. **d**, Schematic illustration of the preparation of T cells and imaging mechanism for MRI. **e**, T₁ phantom images and T₁ maps of T cells with or without T-Fulips treatment at different concentrations of H₂O₂ (+ indicates 50 μM each; - indicates no addition). The data represent the mean ± s.d., analysed by one-way analysis of variance (ANOVA) with post-hoc analysis and two-sided Student's *t*-test; *n* = 3 biologically independent samples; NS represents no significance; **P* < 0.05 and ***P* < 0.01.

microenvironment (Fig. 1a). An increased number of reduced thiol groups (-SH) on the membrane surface of T cells, governed by the reduced form of thioredoxin (Trx)¹⁹ and surface molecules (for example, cluster of differentiation 4 or CD4)²⁰, are associated with the enhanced activity of T cells, and vice versa. The surface redox status of T cells is determined mainly by the local microenvironment rather than the intracellular redox regulatory toolbox of T cells¹⁸. Therefore, the redox status in the tumour microenvironment plays a key role in

regulating the in situ activity of T cells through the oxidation/reduction balance between the -SH and S-S groups²¹, while scavenging extracellular ROS could enhance the responsiveness of T cells and relieve the suppressive immunogenic cell death in tumours²². Taking all this together, we proposed that targeting the surface redox status of T cells could provide a promising way to manage the activity of T cells by cooperating with the oxidative stress in the tumour microenvironment.

Herein, we report a chemical targeting strategy to delineate the activity of T cells by exploiting the balance between –SH and S–S groups on the membrane surface of T cells in the tumour microenvironment (Fig. 1b). We designed T-cell-targeting fusogenic liposomes (T-Fulips), which were composed of ROS-scavenging groups, 2,2,6,6-tetramethylpiperidine (TEMP) and T-cell-targeting anti-CD3 F(ab')₂ fragments conjugated on the particle surface. The T-Fulips could target and fuse with T cells, which leads to the decoration of TEMP groups onto the membrane surface of T cells. As a result, the TEMP groups on the T cells serve as ROS 'decoys', harbouring T cells from the oxidation-induced loss of surface –SH groups, which otherwise would reduce the activity of T cells. Meanwhile, the transformation of diamagnetic TEMP groups into paramagnetic 2,2,6,6-tetramethylpiperidine 1-oxyl (TEMPO) radicals provides prominent changes of the proton T_1 relaxation time for activated magnetic resonance imaging (MRI) quantification of the activity of T cells. Followed by the confirmation of T-Fulips in regulating and imaging the activity of T cells both in vitro and in vivo, we further studied the T-cell-based immune responses by T-Fulips treatment in multiple mouse tumour models. Moreover, we used MRI as a non-invasive and anatomical molecular imaging approach to quantitatively stratify the tumour response by radiation therapy (RT) treatment. This study centred a chemical targeting approach to exploit the in situ activity of T cells for improved cancer theranostics.

T-cell-targeting fusogenic liposomes

We first fabricated TEMP-modified fusogenic liposomes (Fulips) by tuning the ratio between 1,2-dioleoyl-sn-glycero-3-phosphoethanolamine (DOPE), DOPE-PEG₂₀₀₀-TEMP (PEG₂₀₀₀, poly (ethyl glycol)) and 1,2-dioleoyl-3-trimethylammonium propane (DOTAP; Fig. 2a and Supplementary Figs. 1–4). To achieve T cell targeting, T-Fulips were produced by conjugating anti-CD3 F(ab')₂ fragments to the surface of liposomes, while anti-IgGF(ab')₂ fragments were used as an isotope control (denoted as Iso-Fulips). The resulted liposomes (Fulips, T-Fulips and Iso-Fulips) showed vesicular-cup shapes with hydrodynamic diameters of 76.8 ± 12.3 , 80.3 ± 13 and 81.6 ± 16.7 nm, respectively (Fig. 2b and Supplementary Fig. 5). Electrophoresis results further confirmed the successful conjugation of F(ab')₂ fragments on the T-Fulips (Supplementary Fig. 6) with high thermodynamic stability under the physiological conditions (Supplementary Fig. 7).

The T-Fulips showed much higher targeting efficiency to T cells when compared with that of Iso-Fulips (81.4% versus 23.6%; Fig. 2c and Supplementary Fig. 8). The fluorescence resonance energy transfer assay results showed that the T-Fulips without DOTAP (0%) had a relatively low fusion efficiency (14.9%), while increasing the content of DOTAP to 50% in the T-Fulips led to a dramatically increased fusion efficiency of up to 84.3% (Fig. 2d,e and Supplementary Fig. 9). We therefore used the T-Fulips with 50% DOTAP in the following studies. Furthermore, the targeting fusion of T-Fulips to T cells was superior to that of Iso-Fulips with equivalent DOTAP contents (Supplementary Fig. 10).

Greater than 95% of T cells were alive when treated with T-Fulips or Iso-Fulips with concentrations of up to $200 \mu\text{g ml}^{-1}$ (Supplementary Fig. 11), indicating the good biocompatibility of those liposomes. The biodistribution of the T-Fulips in vivo in 4T1 mouse tumours suggested

good tumour targeting and retention effect (Supplementary Fig. 12). In a parallel study, endogenous immune cells were analysed and showed that the percentages of CD8⁺DiR⁺ and CD4⁺DiR⁺ T cells bound with T-Fulips were much higher than those of Iso-Fulips groups (Supplementary Fig. 13a, b). Considering the fact that foreign nanoparticles are mostly engulfed non-specifically by bone-marrow-derived cells^{23,24}, we further analysed the clusters of Gr-1⁺DiR⁺ and F4/80⁺DiR⁺ cells in the above experiments (Supplementary Fig. 13c). The modest interaction of the T-Fulips with lymphocytes could be attributed to the intrinsic lack of Fc for the anti-CD3-F(ab')₂ fragment and the greatly reduced internalization effect^{25,26}. Of particular interest was that the T-Fulips-treated mouse group showed a much lower percentage of F4/80⁺DiR⁺ lymphocytes than that of the Iso-Fulips control (* $P = 0.0457$).

We further investigated the effect of T-Fulips on the proliferation of T cells. T-Fulips without TEMP was defined as T-Lips. The prominent proliferation of T cells ex vivo after a 48 h and 96 h incubation time was achieved for the concanavalin A (conA) + T-Fulips group, which was significantly higher than that of conA + T-Lips (Supplementary Fig. 14). As a result, the secretion of interferon gamma (IFN- γ) by T cells for the conA + T-Fulips group was significantly higher (* $P = 0.0253$) than that of the conA + T-Lips group (Supplementary Fig. 15). Taken together, these results indicate that T-Fulips were able to specifically target and protect T cells from oxidation-induced loss of proliferation efficiency, both in vitro and in vivo.

MRI study of T-Fulips in response to ROS condition

To investigate the MRI performance of T-Fulips in response to ROS, we used H₂O₂ to mimic the oxidative sources in the tumour microenvironment for the oxidation of –SH groups on the membrane surface of T cells. The T_1 -weighted MRI phantoms showed gradually enhanced bright contrast for the T-Fulips with increasing amount of H₂O₂ (Fig. 3a). On the contrary, the T-Fulips samples showed negligible T_1 contrast among different concentrations in the absence of H₂O₂. The semi-quantitative signal-to-noise ratio analysis showed that activated MRI using T-Fulips could provide about twofold enhancement of the signal-to-noise ratio at a typical concentration of $50 \mu\text{M H}_2\text{O}_2$, which further increased with increasing amount of H₂O₂ (Supplementary Fig. 16). Furthermore, the T_1 relaxation time maps were also obtained to quantitatively analyse the T_1 relaxation time changes of T-Fulips with H₂O₂ treatment (Fig. 3b). The MRI results of DOPE-PEG₂₀₀₀-TEMP molecules showed similar trends with those of T-Fulips samples, indicating the major contribution of the T_1 contrast enhancement from TEMPO molecules (Supplementary Fig. 17). The electron paramagnetic resonance measurements further confirmed the formation of paramagnetic TEMPO radicals by H₂O₂ oxidation (Fig. 3c). The T_1 phantom results and relaxation time map analyses indicated that T-Fulips are a good candidate for activatable MRI to delineate the response of T cells to oxidative stress in vitro (Fig. 3d,e).

T-Fulips modulate the proliferation activity of T cells

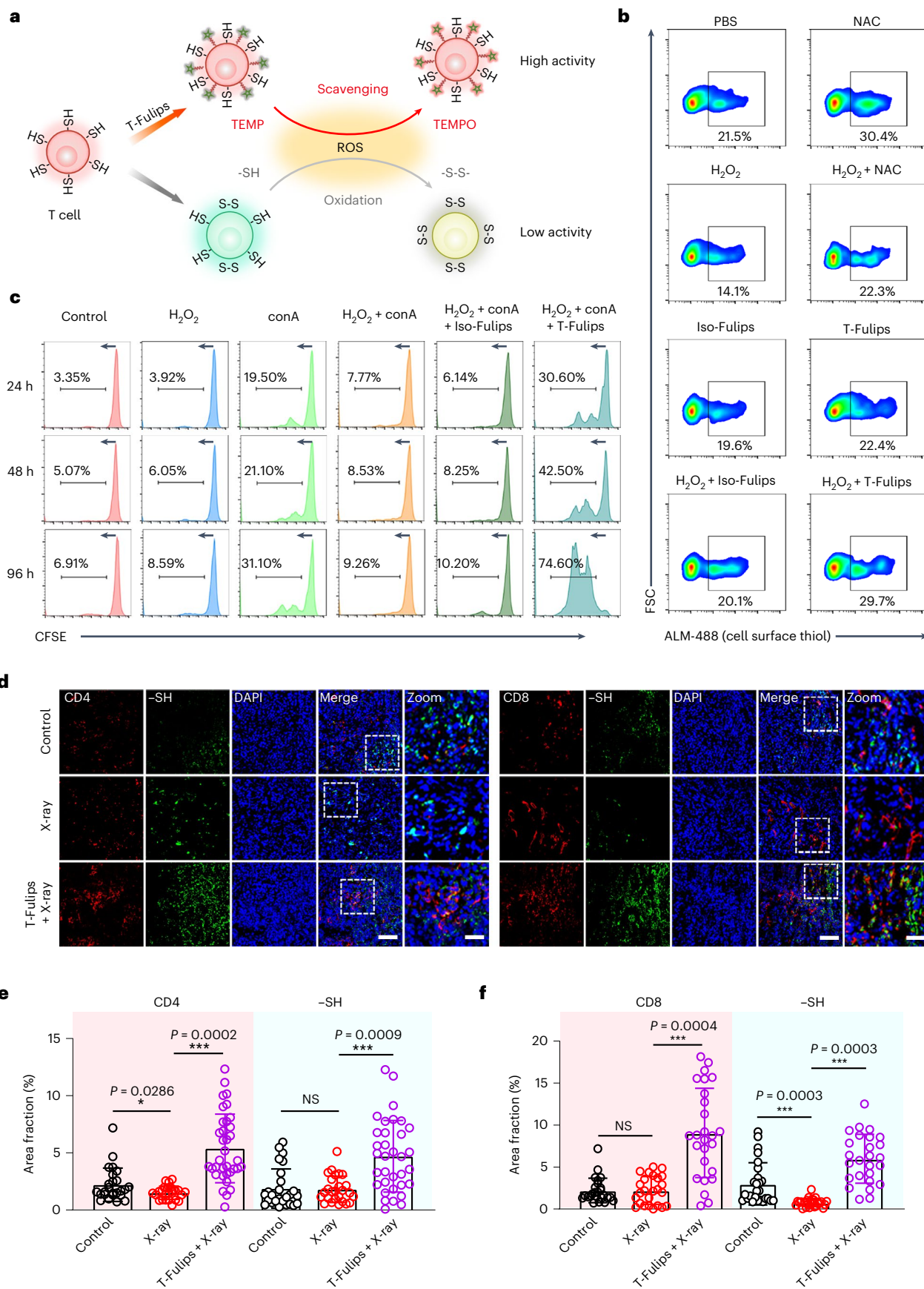
We speculated that the targeting fusion of T-Fulips with T cells could provide ROS 'decoys' on the surface of T cells to resist the oxidation

Fig. 4 | T-Fulips enhance the activity of T cells by regulating –SH groups on the surface. **a**, Schematic illustration of the T-Fulips resisting the oxidation of –SH groups on the surface of T cells. **b**, Flow cytometry analysis of the number of surface –SH groups on T cells under different conditions. *N*-acetylcysteine (NAC) was used as a positive control. Thiol-reactive dye (Alexa Fluor 488 maleimide derivative, ALM-488) was used. PBS, phosphate buffer saline. Data are representative from three biological independent samples. **c**, Flow cytometry analysis of the proliferation efficiency of T cells stimulated with conA, H₂O₂, conA + T-Fulips or Iso-Fulips. Data are representative from five biological independent samples. The arrows showed the displacement direction of the proliferation peak. **d**, Confocal microscopy images of the density of CD4⁺ T cells,

CD8⁺ T cells and –SH groups of the tumours three days after receiving X-ray only or T-Fulips + X-ray treatment. Representative images from random fields of view in one of the three biologically independent mice. The white dashed boxes showed the zoomed area of the tumour. Scale bars of the merge view, $50 \mu\text{m}$; scale bars of the zoom view, $30 \mu\text{m}$. DAPI, 4',6'-diamidino-2-phenylindole. **e**, **f**, Quantitative analysis of the area fractions of the CD4 (red), CD8 (red) and –SH (cyan) signals calculated from the confocal microscopy images. Data were analysed using ImageJ and are shown as the mean \pm s.d.; $n = 5$ random fields of view in one of the five biologically independent mice. Two-sided Student's *t*-test was performed. NS represents no significance; * $P < 0.05$ and *** $P < 0.001$.

of -SH groups on the cell membrane (Fig. 4a). The survival and proliferative behaviour of T cells with T-Fulips treatment were studied by analysing the -SH groups on the membrane of T cells. The results

showed that T-Fulips were able to increase the number of -SH groups on T cells, a number that was comparable to that of an *N*-acetylcysteine treatment group (Fig. 4b). Furthermore, T cells treated with T-Fulips



were able to maintain a high level of surface –SH groups when incubated with H₂O₂ for 48 h, a level which was significantly higher than that of the *N*-acetylcysteine and Iso-Fulips treatment groups (Supplementary Fig. 18). Interestingly, the T-Fulips-treated T cells also showed less intracellular accumulation of ROS as compared with those control groups (Supplementary Fig. 19). These results indicated that the number of surface –SH groups on T cells was inversely correlated with the environmental oxidative potential, which was consistent with the results in the literature¹⁸.

We further investigated whether resisting the ROS-induced oxidation of –SH groups could influence the proliferation activity of T cells. The flow cytometry results showed that H₂O₂ could greatly attenuate the proliferation of T cells even with the presence of conA (Fig. 4c). These results were also consistent with the increased production of IFN- γ and the high number of cell surface –SH groups on T cells, resulting from T-Fulips treatment (Supplementary Figs. 20 and 21). In other words, T-Fulips were able to cultivate a favourable reductive environment on the surface of T cells that prevented the ROS-induced oxidation of –SH groups and rescued T cells from the loss of activity. To explore the relationship between the ratio of thiol to sulfide groups and the T cell functionality, we further studied the proliferation and IFN- γ release of T cells by varying the treatment concentrations of T-Fulips. The results showed that the percentage of surface thiol groups on T cells increased gradually with the concentration of T-Fulips ranging from 6.25 to 100 $\mu\text{g ml}^{-1}$ (Supplementary Fig. 22a, b). The correlation analysis results indicated the presence of an upper limit for surface thiol groups to the T cell functionality (Supplementary Fig. 22c–g). In addition, to exclude the effect of CD3 ϵ ligation to T cells, we prepared anti-CD3 ϵ -coated Fulips without TEMP groups (T-Fulips_{TEMP-free}) as a control to study the T cell functionality after incubation. The results showed minimal changes of the percentage of CFSE^{low} components (CFSE, carboxyfluorescein succinimidyl ester dye; ‘low’ indicates T cells that have lost any level of CFSE labelling) for the T-Fulips_{TEMP-free}-treated T cells compared with those of control groups (Supplementary Fig. 23a). This trend was also consistent with the production of IFN- γ and the cell surface –SH groups on T cells with different treatments (Supplementary Fig. 23b–d).

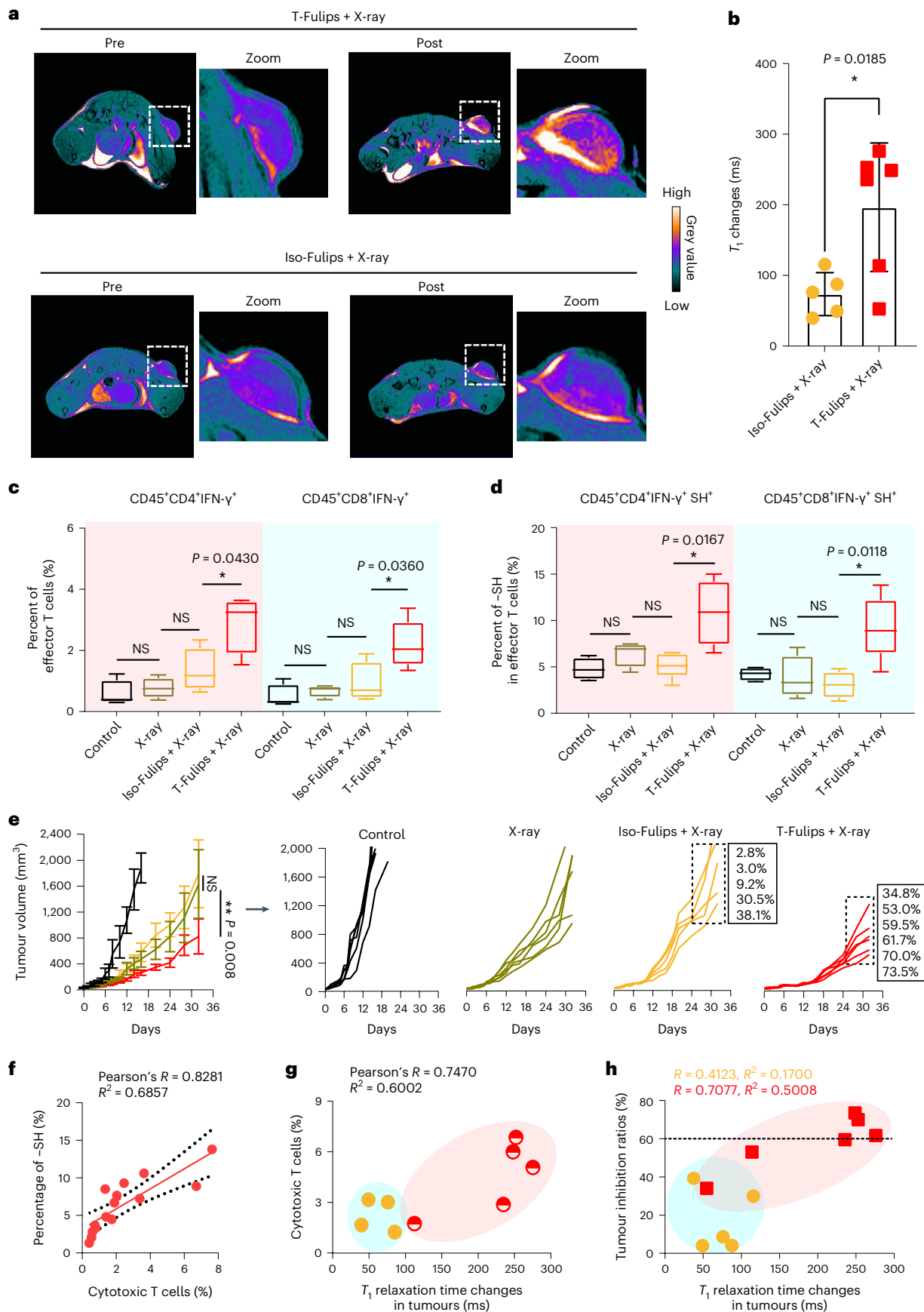
To further study the effectiveness of T-Fulips in modulating the T-cell-based immune response in vivo, we referred to RT in a 4T1 mouse tumour model. The number of CD8⁺ T cells had a significant decrease when the X-ray irradiation dose reached 4 Gy and stayed at a similar level when further increasing the dose to 8 and 12 Gy (Supplementary Fig. 24). Interestingly, the number of CD4⁺ T cells decreased at the irradiation dose of 8 Gy and remained at a similar level when

the radiation dose was further increased. This phenomenon could be due to the different tolerances of CD8⁺ and CD4⁺ T cells in response to irradiation-induced damage^{27,28}. The vulnerability of CD8⁺ T cells further highlighted the importance of managing the activity of CD8⁺ T cells in RT²⁹. We therefore used the irradiation dose of 4 Gy in the following animal studies. The number of tumour-infiltrating helper T cells (CD45⁺CD4⁺IFN- γ ⁺) and cytotoxic T cells (CD45⁺CD8⁺IFN- γ ⁺) gradually increased from day 3 to day 12 after RT (Supplementary Fig. 25, P2 and P5), indicating a time-dependent immune response activated by RT. In particular, we observed a significant decline of both helper and cytotoxic T cells from day 1 to day 3 after RT. However, the number of CD45⁺CD4⁺IFN- γ ⁺ T cells and CD45⁺CD8⁺IFN- γ ⁺ T cells showed little difference between day 1 and day 3 after RT, both of which slightly increased at later time points (Supplementary Fig. 25, P1 and P4). Interestingly, the number of regulatory T (T_{reg}) cells (CD45⁺CD4⁺IFN- γ ⁺FOXP3⁺) decreased significantly during the first three days after RT (Supplementary Fig. 25, P3), indicating that T_{reg} cells were more vulnerable to RT than effector T cells. The double-edged sword effect of RT further implied that the infiltration of T cells could have been compromised with the RT-modulated tumour microenvironment. It has been well documented that RT is accompanied by a large amount of inflammatory ROS production³⁰, which could dampen the survival and proliferative activity of T cells by interacting with the –SH groups on the cell membrane. The tissue immunofluorescence staining results showed that the number of –SH groups decreased significantly at day 3 after RT accompanied with a significantly lower level of tumour-infiltrating CD4⁺/CD8⁺ T cells compared to those of control groups (Fig. 4d–f). Furthermore, the higher rates of infiltrated cytotoxic T cells (CD45⁺CD8⁺IFN- γ ⁺) and helper T cells (CD45⁺CD4⁺IFN- γ ⁺) were observed in the tumours after T-Fulips treatment, especially at day 3 and day 5 after RT, compared with those without T-Fulips treatment (Supplementary Fig. 26). It is interesting that the mouse group treated with T-Fulips but without RT also showed an increased number of tumour-infiltrating T cells at day 3 post-injection, indicating the potential immunomodulatory effect of the T-Fulips. Longitudinally, the number of –SH groups on T cells gradually increased from day 1 to day 5 after RT, which positively correlated with the 1.9-fold and 2.8-fold increases of the CD4⁺ and CD8⁺ T cells, respectively, in the tumour (Supplementary Fig. 27). Taken together, these results indicate that T-Fulips were able to resist ROS-induced oxidation of –SH groups on the membrane surface of T cells, which could be a promising strategy for nurturing a favourable microenvironment for the proliferation of T cells both in vitro and in vivo.

Fig. 5 | T-Fulips regulate and quantify the activity of T cells in the RT of a mouse 4T1 tumour model.

a, T₁ MRI pseudo-colour images of mouse treated with T-Fulips + X-ray (upper) and Iso-Fulips + X-ray (lower). The white dashed squares show the zoomed-in area of the tumours. **b**, Quantitative T₁ relaxation time changes in mouse tumours of different groups ($n = 5$ or 6 per group). Data are shown as the mean \pm s.d., and a two-sided Student's *t*-test was performed. * $P < 0.05$. Data colours in **b** are related to the colours in the subsequent panels. Dots or squares with the same colour represent same group. Orange is for ‘Iso-Fulips + X-ray’ group. Red is for ‘T-Fulips + X-ray’ group. **c**, Quantification of CD45⁺CD8⁺IFN- γ ⁺ (red) and CD45⁺CD4⁺IFN- γ ⁺ (cyan) cells in tumours after different treatments ($n = 5$ per group). The box plot displays the first and third quartiles (top and bottom of the boxes), the median (band inside the boxes) and the lowest and highest point within 1.5 times the interquartile range of the lower and higher quartile (whiskers). Data are shown as the mean \pm s.d.; two-sided Student's *t*-test was performed; * $P < 0.05$. **d**, Percentages of –SH groups on effector T cells ($n = 5$ per group). CD45⁺CD8⁺IFN- γ ⁺SH⁺ (red) and CD45⁺CD4⁺IFN- γ ⁺SH⁺ (cyan) are shown. The box plot displays the first and third quartiles (top and bottom of the boxes), the median (band inside the boxes) and the lowest and highest point within 1.5 times the interquartile range of the lower and higher quartile (whiskers). Data are shown as the mean \pm s.d.; two-sided Student's *t*-test was performed; * $P < 0.05$. **e**, Tumour growth curves of mouse

groups with different treatments, including control, X-ray, Iso-Fulips + X-ray and T-Fulips + X-ray. Individual tumour growth curves and the corresponding tumour inhibition rates (data inside dashed boxes) are shown. The tumour growth inhibition rates were calculated by the following equation: $\{1 - [(exp_{\text{end point}} - exp_{\text{day0}}) / (\text{control}_{\text{day16}} - \text{control}_{\text{day0}})]\} \times 100$. exp, experimental group. Data are shown as the mean \pm s.d.; two-sided Student's *t*-test was performed. NS represents no significance; ** $P < 0.01$. **f**, Correlations between the percent of –SH groups and the corresponding proportions of cytotoxic T cells for individual mice from different treatment groups. The red dots represent the percentage of cytotoxic T cells and proportion of –SH groups corresponding to individual mice. The Pearson's correlation coefficient *R* is 0.8281. Red line: best linear fit (slope is significantly different from zero, 95% confidence interval), dotted lines: 95% confidence interval. **g**, Correlations between the T₁ relaxation time changes and the cytotoxic T cells of mouse groups receiving Iso-Fulips + X-ray (orange dots) and T-Fulips + X-ray (half-red dots). The Pearson's correlation coefficient *R* is 0.7470. **h**, Correlations between the T₁ relaxation time changes and tumour inhibition rates for mice treated with Iso-Fulips + X-ray (orange dots) and T-Fulips + X-ray (red squares), showing the Pearson's correlation coefficient *R* of 0.4123 and 0.7077, respectively. The horizontal black dashed line indicates 60% tumour volume inhibition rate.



T-Fulips regulate immune response and predict therapeutic outcomes

Next, we studied the ability of T-Fulips in delineating the change of T cells using quantitative MRI in a 4T1 murine tumour model. We acquired the T_1 images of tumours at pre- and post-contrast time points in two groups with T-Fulips or Iso-Fulips treatment before RT (Fig. 5a and Supplementary Fig. 28). The results showed that mice treated with T-Fulips 24 h before RT had a prominent T_1 relaxation time change in the tumours, which was significantly higher than that of Iso-Fulips: 197.3 ± 81.5 ms versus 74.1 ± 31.6 ms ($*P = 0.0185$), respectively (Fig. 5b). Similar results were obtained for two groups treated with T-Fulips or Iso-Fulips after RT: X-ray + T-Fulips (248.3 ± 64.6 ms) and X-ray + Iso-Fulips (61.8 ± 34.2 ms), respectively (Supplementary Figs. 29 and 30). The histology staining showed the well-matched spatial distribution between CD3⁺ T cells and T-Fulips in the tumours (Supplementary Fig. 31), further indicating the efficient targeting of T-Fulips to CD3⁺ T cells in vivo. In addition, the CD3⁺ T cells isolated from the tumours after T-Fulips treatment showed prominent electron paramagnetic resonance signals (Supplementary Fig. 32), indicating the existence of paramagnetic TEMPO radicals on T cells. Those results demonstrated that the change of T_1 relaxation time in MRI was attributed to CD3⁺ T cells in the tumours.

Furthermore, the analysis of the retrieved CD45⁺CD4⁺IFN- γ ⁺ and CD45⁺CD8⁺IFN- γ ⁺ cells from the tumours at day 12 post-RT showed that mouse tumours with T-Fulips and RT treatments, regardless of the order of the treatments, had higher levels of activated T cells and a greater number of -SH groups in the tumours compared with those of Iso-Fulips groups (Fig. 5c,d and Supplementary Figs. 33 and 34). The ROS-scavenging effect of the T-Fulips could suppress the expression of thioredoxin-interacting protein, which, as a result, sustained the activity of thioredoxin and the number of surface -SH groups (Supplementary Fig. 35). Interestingly, the high level of Trx upon T-Fulips treatment was also associated with the augmented intracellular level of antioxidant defenses including Trx, thioredoxin reductase (TrxR) and glutathione (GSH). This phenomenon indicated that resisting the ROS-induced oxidation of -SH groups could modulate the intracellular redox balance, which subsequently shaped the survival and proliferation activity of T cells. Enzyme-linked immunosorbent assay (ELISA) measurements at day 12 after RT showed that the mouse groups with T-Fulips and X-ray treatments had a significantly higher level of interleukin-6 (IL-6), granzyme B (Gzms-B), tumour necrosis factor- α (TNF- α) and IFN- γ in the plasma compared with those treated with Iso-Fulips and X-ray treatment (Supplementary Fig. 36). The tumour growth curves, the mouse body weights and the survival rates of mouse groups were recorded until at least 32 days after the different treatments (Fig. 5e and Supplementary Figs. 37 and 38). The results showed that the two mouse groups treated with T-Fulips and X-ray, regardless of the treatment order, had greatly improved survival rates (58.8% and 54.4% on average) compared with those of the Iso-Fulips groups (16.7% and 40.9% on average). The minimal changes of the alanine aminotransferase and aspartate aminotransferase levels in the plasma and the serum levels of uric acid, urea, creatinine, creatine kinase, creatine kinase isoenzyme myocardial band and lactate dehydrogenase indicate

the low systemic toxicity of the different treatments (Supplementary Fig. 39a–h). In addition, the hematoxylin and eosin staining results of major organs including heart, liver, spleen, lung and kidneys at day 12 after T-Fulips treatment further support the good biocompatibility of our materials (Supplementary Fig. 39i).

We further analysed the correlation between the percentages of -SH groups and the amounts of cytotoxic T cells in tumours of mice at day 12 after different treatments, showing the Pearson's correlation coefficient R of 0.8281 ($R^2 = 0.6857$; Fig. 5f). The Pearson's R correlation between the T_1 relaxation time changes at day 2 and the number of cytotoxic T cells at day 12 in the tumours after different treatments (T-Fulips or Iso-Fulips followed by X-ray irradiation) was 0.7470 ($R^2 = 0.6002$; Fig. 5g). More importantly, the Pearson's R correlation between the T_1 relaxation time changes and the tumour growth inhibition rates was 0.7077 ($R^2 = 0.5008$) for the T-Fulips + X-ray treated mouse group (Fig. 5h). The Pearson's R value was 0.9599 ($R^2 = 0.9214$) for the X-ray + T-Fulips treated mouse group (Supplementary Fig. 40). Furthermore, T-Fulips showed similar tumour inhibition efficiencies and prognostic capabilities in an MC-38 murine tumour model, indicating the generality of T-Fulips and the MRI approach in cancer theranostics (Supplementary Fig. 41).

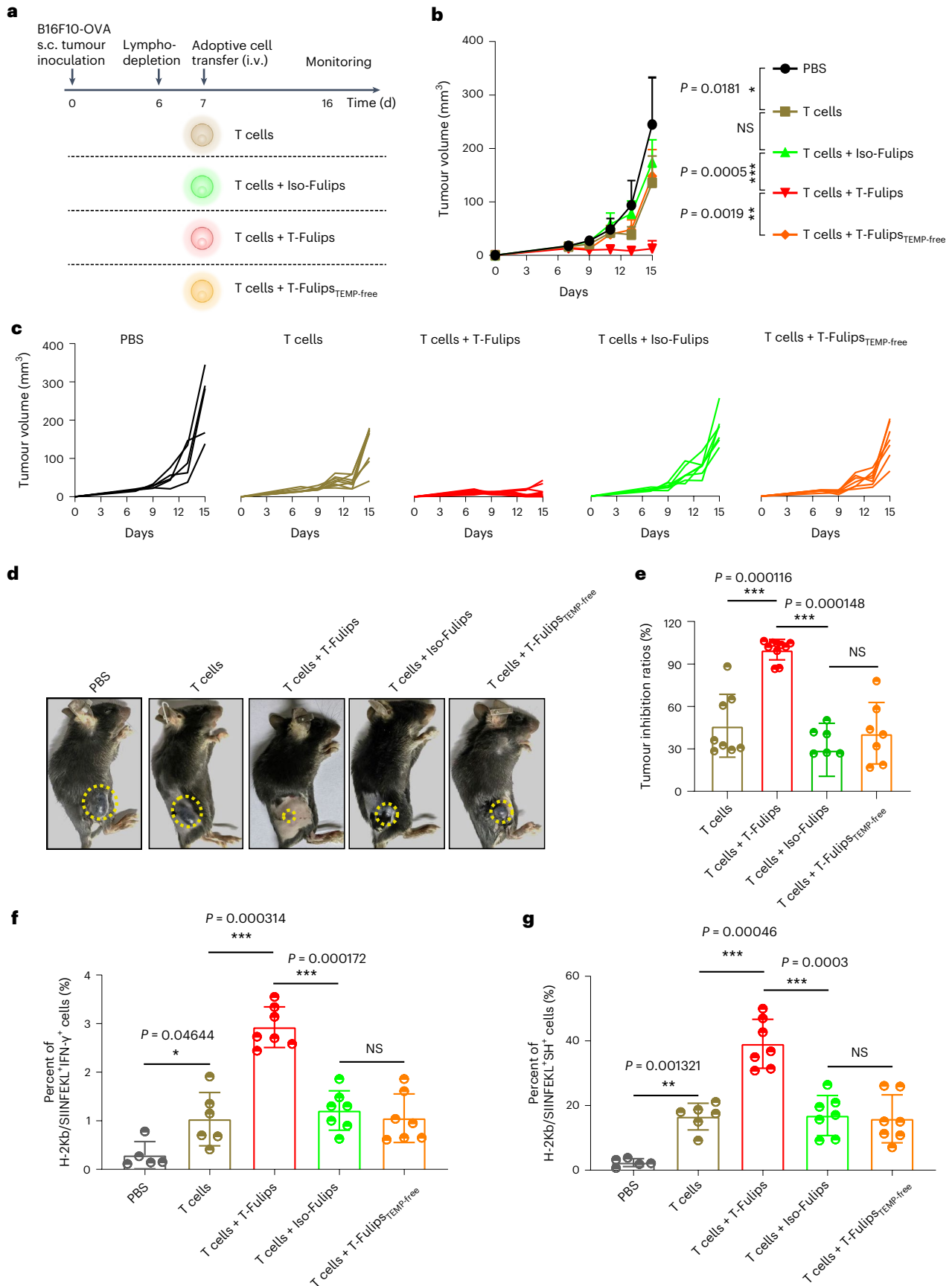
In addition, we studied the efficacy of T-Fulips in regulating the activity of T cells in an adoptive cell therapy tumour model. Although adoptive cell therapy has shown great clinical impact on treating haematological cancers, the therapeutic outcome of adoptive cell therapy in solid tumours remains elusive^{31,32}. We anticipated that the redox status of the tumour microenvironment might take part in the activity of tumour-infiltrated T cells through oxidizing the surface -SH groups on the T cells. In this respect, T cells pre-incubated with T-Fulips may hold great potential in preventing surface oxidation in the tumour microenvironment for improved tumoricidal effect. The results showed that activated OT-I CD8⁺ T cells treated with T-Fulips greatly reduced the proliferation rate of B16F10-OVA cells in vitro both in the presence and in the absence of H₂O₂ (Supplementary Fig. 42a). By contrast, OT-I CD8⁺ T cells incubated with Iso-Fulips or T-Fulips_{TEMP-free} showed a limited effect on the proliferation of B16F10-OVA cells with enhanced Ki67^{high} expression (where 'high' indicates a larger number of proliferating cells). The increased production of IFN- γ from T cells further confirmed the improved activity of T cells by T-Fulips treatment in vivo (Supplementary Fig. 42b, c).

To investigate whether T-Fulips could promote the therapeutic efficacy of T cells in vivo, T cells pretreated with T-Fulips were intravenously (i.v.) injected into B16F10-OVA mouse tumour groups (Fig. 6a). The tumour growth for different groups was monitored, and the T cells + T-Fulips group showed great tumour inhibition efficiency (100.1%) compared with those of control groups: 29.4% ($***P = 0.000148$) and 41.1% ($***P = 0.000116$) for Iso-Fulips and T-Fulips_{TEMP-free}, respectively (Fig. 6b–e). Flow cytometry analysis of the antigen-specific H-2Kb/SIINFEKL⁺IFN- γ ⁺ T cells in the tumours harvested on the end-point day showed that mice receiving T cells + T-Fulips treatment had higher levels of effector T cells and a greater number of -SH groups in the tumours compared with those of the T cell only, Iso-Fulips and T-Fulips_{TEMP-free} groups (Fig. 6f,g and

Fig. 6 | T-Fulips promote the therapeutic efficacy of adoptive T cell therapy in a B16F10-OVA model. **a**, Experimental design of the study. B16F10-OVA tumour cells were injected subcutaneously (s.c.) into C57BL/6 mice to establish the tumour model. Mice were then sub-lethally lymphodepleted by irradiation on day 6 and intravenously administered activated OT-I CD8⁺ T cells on day 7. Mouse groups were injected with PBS, T cells, T cells + Iso-Fulips, T-Fulips or T-Fulips_{TEMP-free} (T-Fulips without TEMP). **b,c**, Curves show the averaged and the individual tumour growth profiles for different groups ($n = 5-7$ per group). Averaged data are shown as the mean \pm s.d.; two-sided Student's t -test was performed. $*P < 0.05$, $**P < 0.01$ and $***P < 0.001$. **d**, Representative C57BL/6 mouse images acquired on the end-point day. The tumours are outlined with yellow dotted circles.

e, Quantitative tumour inhibition rates of mouse groups with different treatments ($n = 5-7$ per group). Data are shown as the mean \pm s.d.; two-sided Student's t -test was performed. NS represents no significance; $***P < 0.001$. **f**, Quantification of the antigen-specific H-2Kb/SIINFEKL⁺IFN- γ ⁺ T cells in the tumours after different treatments ($n = 5-7$ per group). Data are shown as the mean \pm s.d.; two-sided Student's t -test was performed. NS represents no significance; $*P < 0.05$ and $***P < 0.001$. **g**, Percentages of -SH groups on the antigen-specific H-2Kb/SIINFEKL⁺IFN- γ ⁺ T cells ($n = 5-7$ per group). Data are shown as the mean \pm s.d.; two-sided Student's t -test was performed. NS represents no significance; $**P < 0.01$ and $***P < 0.001$.

Supplementary Fig. 43). The incubation of T cells with T-Fulips or T-Fulips_{TEMP-free} did not alter the accumulation efficiency of T cells in the mouse B16F10-OVA tumours (Supplementary Fig. 44), which confirmed the critical role of TEMP groups in regulating the surface redox status of T cells for improved therapeutic outcomes. Furthermore, these results highlight that T-Fulips treatment is an effective means to manage the



activity of T cells in the tumour microenvironment for improved cancer immunotherapy.

Conclusion

Mounting evidence has shown that the functional activity and proliferation of T cells require an optimal reductive microenvironment^{33–35}, in which the redox balance between –SH and S–S groups on the membrane surface of T cells plays an important role¹⁸. During cancer progression, however, tumours are often cultivated with oxidative stress, which may cause the oxidation of the –SH groups into S–S groups on the surface of the T cells, resulting in the loss of activity of the T cells. This phenomenon partially contributes to the immunosuppressive nature of cancers, which potentiates the administration of antioxidant molecules (such as Trx and vitamins) and the use of cytokines and anti-inflammatory drugs to enhance the response of T cells, with varied success^{19,36,37}. In a recent study, adjuvant drug delivery aided by the surface reductive environment of T cells was applied to improve the efficacy of an adoptive T cell cancer therapy³⁸. In our work, we employed a nanomaterial approach to regulate and quantify the activity of T cells by targeting the redox status on the membrane surface of T cells. The favourable reductive microenvironment with an increased number of –SH groups on the surface of the T cells after T-Fulips treatment was linked to the greatly improved survival and proliferation activity of the T cells. Meanwhile, this procedure led to a paramagnetic transition of TEMP to TEMPO molecules, allowing for quantitative stratification of the tumour response by activated MRI for an early prognosis of RT.

A plethora of molecular imaging methods targeting the specific biomarkers (for example, OX40 and major histocompatibility complex (MHC)-encoded products) of T cells through non-covalent or covalent binding approaches have been reported^{39–41}. However, the relationship between the number of biomarkers and the dynamic activity of T cells is still debatable. In the current work, we surmised that the chemical strategy of regulating the redox status on the surface of T cells is amenable to explain the trade-off between the expression of biomarkers and the ROS-induced oxidative stress. This approach is beneficial to systematically improve the immunotherapy response and to quantitatively stratify the pathological progress related to the immune activation of T cells in the tumour. Emerging evidence has shown that exhausted T cells, a subpopulation of cell dysfunction, present one of the major hurdles to cancer immunotherapy⁴². Although the mechanism is largely unknown, it was found that ROS accumulation is one of the characteristic features of exhausted T cells⁴³. This phenomenon is also supported by our results, shown in the Supplementary Fig. 19, indicating that the redox stress response was essential to shift the balance towards the activity of T cells. Although we mainly referred to the effector T cells, T_{regs} would also benefit from surface redox regulation by T-Fulips treatment through a transforming growth factor beta (TGF- β)-dependent mechanism^{44–46}. Furthermore, we speculate that targeting the redox metabolism by chemical approaches could be fruitful to regulate the fate of a variety of immune cells, such as B cells, dendritic cells, natural killer cells, macrophages and neutrophils. Hence, targeting the activity of immune cells could be promising to the management of many diseases that are related to the activation of immune cells, such as virus infection (for example, COVID-19)⁴⁷, chronic inflammatory diseases⁴⁸, rheumatoid arthritis⁴⁹ and so on.

In conclusion, we have presented a chemical targeting strategy to delineate the activity of T cells by exploiting the surface redox status both in vitro and in vivo. The developed T-Fulips were equipped with TEMP groups to neutralize ROS and protect T cells from an oxidation-induced loss of activity. Meanwhile, the production of paramagnetic TEMPO radicals allowed MRI quantification of the T cell activity. This study uses a chemical targeting strategy to regulate the in situ activity of T cells in a visualizable manner for cancer theranostics and may provide further understanding on engineering T cells for cancer treatment.

Online content

Any methods, additional references, Nature Portfolio reporting summaries, source data, extended data, supplementary information, acknowledgements, peer review information; details of author contributions and competing interests; and statements of data and code availability are available at <https://doi.org/10.1038/s41565-022-01261-7>.

References

- Melero, I., Castanon, E., Alvarez, M., Champiat, S. & Marabelle, A. Intratumoural administration and tumour tissue targeting of cancer immunotherapies. *Nat. Rev. Clin. Oncol.* **18**, 558–576 (2021).
- Lyu, L., Feng, Y., Chen, X. & Hu, Y. The global chimeric antigen receptor T (CAR-T) cell therapy patent landscape. *Nat. Biotechnol.* **38**, 1387–1394 (2020).
- Nagarsheth, N. B. et al. TCR-engineered T cells targeting E7 for patients with metastatic HPV-associated epithelial cancers. *Nat. Med.* **27**, 419–425 (2021).
- Gong, N., Sheppard, N. C., Billingsley, M. M., June, C. H. & Mitchell, M. J. Nanomaterials for T-cell cancer immunotherapy. *Nat. Nanotechnol.* **16**, 25–36 (2021).
- Morotti, M. et al. Promises and challenges of adoptive T-cell therapies for solid tumours. *Brit. J. Cancer* **124**, 1759–1776 (2021).
- Galluzzi, L., Chan, T. A., Kroemer, G., Wolchok, J. D. & López-Soto, A. The hallmarks of successful anticancer immunotherapy. *Sci. Transl. Med.* **10**, eaat7807 (2018).
- Levi, J. et al. Imaging of activated T cells as an early predictor of immune response to anti-PD-1 therapy. *Cancer Res.* **79**, 3455–3465 (2019).
- Shi, C., Zhou, Z., Lin, H. & Gao, J. Imaging beyond seeing: early prognosis of cancer treatment. *Small Methods* **5**, 2001025 (2021).
- Nishino, M., Hatabu, H. & Hodi, F. S. Imaging of cancer immunotherapy: current approaches and future directions. *Radiology* **290**, 9–22 (2018).
- Scheper, W. et al. Low and variable tumor reactivity of the intratumoral TCR repertoire in human cancers. *Nat. Med.* **25**, 89–94 (2019).
- Galon, J. et al. Type, density, and location of immune cells within human colorectal tumors predict clinical outcome. *Science* **313**, 1960–1964 (2006).
- Zhang, L. et al. Intratumoral T cells, recurrence, and survival in epithelial ovarian cancer. *New Engl. J. Med.* **348**, 203–213 (2003).
- Quail, D. F. & Joyce, J. A. Microenvironmental regulation of tumor progression and metastasis. *Nat. Med.* **19**, 1423–1437 (2013).
- Jin, M.-Z. & Jin, W.-L. The updated landscape of tumor microenvironment and drug repurposing. *Signal Transduct. Target Ther.* **5**, 166 (2020).
- Gong, N. et al. Carbon-dot-supported atomically dispersed gold as a mitochondrial oxidative stress amplifier for cancer treatment. *Nat. Nanotechnol.* **14**, 379–387 (2019).
- Tang, L. et al. Targeting neutrophils for enhanced cancer theranostics. *Adv. Mater.* **32**, 2002739 (2020).
- Zanganeh, S. et al. Iron oxide nanoparticles inhibit tumour growth by inducing pro-inflammatory macrophage polarization in tumour tissues. *Nat. Nanotechnol.* **11**, 986–994 (2016).
- Gelderman, K. A., Hultqvist, M., Holmberg, J., Olofsson, P. & Holmdahl, R. T cell surface redox levels determine T cell reactivity and arthritis susceptibility. *Proc. Natl Acad. Sci. USA* **103**, 12831–12836 (2006).
- Chakraborty, P. et al. Thioredoxin-1 improves the immunometabolic phenotype of antitumor T cells. *J. Biol. Chem.* **294**, 9198–9212 (2019).
- Hogg, P. J. Disulfide bonds as switches for protein function. *Trends Biochem. Sci.* **28**, 210–214 (2003).

21. Sahaf, B., Heydari, K., Herzenberg, L. A. & Herzenberg, L. A. Lymphocyte surface thiol levels. *Proc. Natl Acad. Sci. USA* **100**, 4001–4005 (2003).
22. Deng, H. et al. Targeted scavenging of extracellular ROS relieves suppressive immunogenic cell death. *Nat. Commun.* **11**, 4951 (2020).
23. Gustafson, H. H., Holt-Casper, D., Grainger, D. W. & Ghandehari, H. Nanoparticle uptake: the phagocyte problem. *Nano Today* **10**, 487–510 (2015).
24. Sousa de Almeida, M. et al. Understanding nanoparticle endocytosis to improve targeting strategies in nanomedicine. *Chem. Soc. Rev.* **50**, 5397–5434 (2021).
25. Schmid, D. et al. T cell-targeting nanoparticles focus delivery of immunotherapy to improve antitumor immunity. *Nat. Commun.* **8**, 1747 (2017).
26. Arlauckas, S. P. et al. In vivo imaging reveals a tumor-associated macrophage-mediated resistance pathway in anti-PD-1 therapy. *Sci. Transl. Med.* **9**, eaal3604 (2017).
27. Ozsahin, M. et al. CD4 and CD8 T-lymphocyte apoptosis can predict radiation-induced late toxicity: a prospective study in 399 patients. *Clin. Cancer Res.* **11**, 7426–7433 (2005).
28. Wilkins, R. C., Kutzner, B. C., Truong, M. & McLean, J. R. N. The effect of the ratio of CD4⁺ to CD8⁺ T-cells on radiation-induced apoptosis in human lymphocyte subpopulations. *Int. J. Radiat. Biol.* **78**, 681–688 (2002).
29. Weichselbaum, R. R., Liang, H., Deng, L. & Fu, Y. X. Radiotherapy and immunotherapy: a beneficial liaison? *Nat. Rev. Clin. Oncol.* **14**, 365–379 (2017).
30. Zhou, Z. et al. Early stratification of radiotherapy response by activatable inflammation magnetic resonance imaging. *Nat. Commun.* **11**, 3032 (2020).
31. Restifo, N. P., Dudley, M. E. & Rosenberg, S. A. Adoptive immunotherapy for cancer: harnessing the T cell response. *Nat. Rev. Immunol.* **12**, 269–281 (2012).
32. Hammerl, D., Rieder, D., Martens, J. W. M., Trajanoski, Z. & Debets, R. Adoptive T cell therapy: new avenues leading to safe targets and powerful allies. *Trends Immunol.* **39**, 921–936 (2018).
33. Angelini, G. et al. Antigen-presenting dendritic cells provide the reducing extracellular microenvironment required for T lymphocyte activation. *Proc. Natl Acad. Sci. USA* **99**, 1491–1496 (2002).
34. Muri, J. & Kopf, M. Redox regulation of immunometabolism. *Nat. Rev. Immunol.* **21**, 363–381 (2021).
35. Hildeman, D. A., Mitchell, T., Kappler, J. & Murrack, P. T cell apoptosis and reactive oxygen species. *J. Clin. Invest.* **111**, 575–581 (2003).
36. Kouakanou, L. et al. Vitamin C promotes the proliferation and effector functions of human $\gamma\delta$ T cells. *Cell. Mol. Immunol.* **17**, 462–473 (2020).
37. Pelly, V. S. et al. Anti-inflammatory drugs remodel the tumor immune environment to enhance immune checkpoint blockade efficacy. *Cancer Discov.* **11**, 2602–2619 (2021).
38. Tang, L. et al. Enhancing T cell therapy through TCR-signaling-responsive nanoparticle drug delivery. *Nat. Biotechnol.* **36**, 707–716 (2018).
39. Alam, I. S. et al. Imaging activated T cells predicts response to cancer vaccines. *J. Clin. Invest.* **128**, 2569–2580 (2018).
40. Woodham, A. W. In vivo detection of antigen-specific CD8⁺ T cells by immuno-positron emission tomography. *Nat. Methods* **17**, 1025–1032 (2020).
41. Tavare, R. et al. An effective immuno-PET imaging method to monitor CD8-dependent responses to immunotherapy. *Cancer Res.* **76**, 73–82 (2016).
42. Guo, Y. et al. Metabolic reprogramming of terminally exhausted CD8⁺ T cells by IL-10 enhances anti-tumor immunity. *Nat. Immunol.* **22**, 746–756 (2021).
43. Scharping, N. E. et al. Mitochondrial stress induced by continuous stimulation under hypoxia rapidly drives T cell exhaustion. *Nat. Immunol.* **22**, 205–215 (2021).
44. Kraaij, M. D. et al. Induction of regulatory T cells by macrophages is dependent on production of reactive oxygen species. *Proc. Natl Acad. Sci. USA* **107**, 17686–17691 (2010).
45. Yan, Z., Garg, S. K., Kipnis, J. & Banerjee, R. Extracellular redox modulation by regulatory T cells. *Nat. Chem. Biol.* **5**, 721–723 (2009).
46. Blakytyn, R., Erkell, L. J. & Brunner, G. Inactivation of active and latent transforming growth factor beta by free thiols: potential redox regulation of biological action. *Int. J. Biochem. Cell Biol.* **38**, 1363–1373 (2006).
47. Laforge, M. et al. Tissue damage from neutrophil-induced oxidative stress in COVID-19. *Nat. Rev. Immunol.* **20**, 515–516 (2020).
48. Furman, D. et al. Chronic inflammation in the etiology of disease across the life span. *Nat. Med.* **25**, 1822–1832 (2019).
49. Wright, H. L., Moots, R. J. & Edwards, S. W. The multifactorial role of neutrophils in rheumatoid arthritis. *Nat. Rev. Rheumatol.* **10**, 593–601 (2014).

Publisher's note Springer Nature remains neutral with regard to jurisdictional claims in published maps and institutional affiliations.

Springer Nature or its licensor (e.g. a society or other partner) holds exclusive rights to this article under a publishing agreement with the author(s) or other rightsholder(s); author self-archiving of the accepted manuscript version of this article is solely governed by the terms of such publishing agreement and applicable law.

© The Author(s), under exclusive licence to Springer Nature Limited 2022

Methods

Preparation of fusogenic liposomes

Liposomes were prepared according to the method described by Csiszár et al.⁵⁰ with slight modifications. Briefly, lipid components DOPE, DOPE-PEG₂₀₀₀-Maleimide (MAL), DOPE-PEG₂₀₀₀-TEMP and positively charged lipid DOTAP and the fluorescent compound DiR were mixed in chloroform at a molar ratio of 1:0.12:0.12:1:0.12. Chloroform was evaporated under a vacuum for 0.5 h. Then, lipids were dispersed in PBS at a total lipid concentration of 2 mg ml⁻¹ at pH 7.4. The solution was vortexed for 2 min to produce multilamellar liposomes. After homogenization in an ultrasonic bath for 20 min at 4 °C, mainly unilamellar vesicles were formed. Characterization of the size and zeta potential distribution of liposomes was conducted by transmission electron microscopy, dynamic light scattering and electrophoretic light scattering.

Antibody conjugation

CD3⁺ T-cell-specific Fulips were generated by conjugating anti-CD3ε monoclonal antibody F(ab')₂ fragments to the particle surface. Anti-IgG-F(ab')₂ fragments were used as the isotype control. The antibody fragments were reduced using 2 mM dithiothreitol for 90 min at 25 °C to retrieve free sulfhydryl groups for chemical linkage to the maleimide groups on the nanoparticle surface. Free dithiothreitol was removed before conjugation using 7 kDa desalting columns. Some 50 µg of antibody was added per 1 mg of liposomes. The reaction was carried out for 12 h at 25 °C under nitrogen protection, and then purified by two wash-spin cycles in PBS at 70,000 g for 60 min. The amount of antibody on the nanoparticle surface was quantified by bicinchoninic acid (BCA) assay. The amount of F(ab')₂ fragments on the surface of T-Fulips and Iso-Fulips was ~30 µg per mg of the liposome samples.

Cell culture and animal tumour model

The 4T1, MC-38 cells were acquired from the American Type Culture Collection. B16F10-OVA cells were from Cell Bank of Shanghai, Chinese Academy of Sciences. Cells were cultured in Dulbecco's modified Eagle's medium (DMEM) containing 10% heat-inactivated foetal bovine serum (FBS) and supplemented to a final concentration with L-glutamine (2 mM), penicillin (50 U ml⁻¹) and streptomycin (50 µg ml⁻¹). Murine T cells were enriched from spleens using a mouse CD3 T cell isolation kit and cultured in RPMI-1640 medium supplemented with 10% FBS and 1% penicillin-streptomycin. The purity of the isolated cells was determined using anti-mouse CD3 antibody and confirmed to be greater than 95% pure. Animals were housed in groups of 4–5 mice per cage, maintained at a temperature of ~25 °C in a humidity-controlled environment with a 12 h light/dark cycle. To establish the tumour model, BALB/c mice were subcutaneously inoculated with 1 × 10⁶ 4T1 tumour cells on the right flank. C57BL/6 mice were subcutaneously inoculated with 1 × 10⁶ MC-38 or B16F10-OVA tumour cells on the right flank. All animal experiments were carried out in accordance with the Guide Protocol of Laboratory Animals, approved by the Ethics Committee of Xiamen University. Six- to eight-week-old female BALB/c mice were ordered from the Xiamen University and Guangzhou Medical University Animal Centers.

In vitro T cell assays

In vitro binding of Fulips was assessed after incubation of 30,000 enriched CD3 T cells with DiR-fluorescent-dye-labelled liposomes at different concentrations for 30 min at 37 °C. After the incubation, T cells were washed three to five times in PBS and directly assessed by flow cytometry and laser scanning confocal microscopy for DiR fluorescence. For internalization studies, cells were incubated for different periods of time on ice, washed and stained immediately with LysoTracker staining. For the T cell proliferation assay, the murine T cells were collected and labelled with CFSE (0.5 mM) for 5 min. Then,

conA and H₂O₂ were added. After one to three days, the CFSE signal was analysed by a flow cytometer. For the measurement of -SH groups, ALM-488 was used at the indicated concentrations, and the fluorescence of -SH staining was determined by flow cytometry.

Biodistribution of the T-Fulips

The 4T1 tumour model was established in BALB/c mice. When the tumours had grown to around 100 mm³ (tumour volume = ½ × length × width²), T-Fulips or isotype control were administered intravenously. Mice were anaesthetized and imaged using a Carestream Imaging Station system at 1, 4, 6, 12, 24 and 48 h post-injection. At the last time point, mice were killed. Tumour and normal organs including heart, liver, spleen, lung, kidneys and brain were dissected for ex vivo imaging.

MRI measurements and analysis

All phantoms and animal MRI studies were performed on a 9.4 T small animal MRI scanner (Bruker 94/20). The phantom samples with different concentrations of DOPE-PEG₂₀₀₀-TEMP and T-Fulips were prepared in solution with the addition of different amounts of H₂O₂. For animal studies, all the mice were anaesthetized with an isoflurane/O₂ mixture and placed in a stretched prone position. T₁ MRI experiments were acquired using a rapid acquisition with relaxation enhancement with variable repetition time sequence. The T₁ MRI phantoms were acquired using the following parameters: effective echo time (TE), 8.50 ms; flip angle, 180°; rare factor, 2; slice thickness, 1 mm; field of view, 3.0 cm × 3.0 cm; number of repetitions, 1; number of averages, 2; and matrix, 256 × 256. For the activated MRI, the T-Fulips or Iso-Fulips were injected intravenously with an injection dose of 10 mg per kilogram mouse body weight. The post-contrast MRI was acquired 24 h after the injection of contrast agents using the same sequence parameters as those for the pre-contrast T₁ MRI study. All the simulations of T₁ maps were calculated on a pixel-by-pixel basis using the built-in software (Paravision 5.1, Bruker). Regions of interest were manually drawn across images. The quantitative T₁ maps were calculated from the multi-TR signals with nonlinear least square fitting of the data with the following equation: $M(\text{TR}) = M_0 \left[1 - \exp\left(-\frac{\text{TR}}{T_1}\right) \right]$, where $M(\text{TR})$ is the signal intensity at each TR, M_0 is a free fitting variable equal to $M(\text{TR} = +\text{inf})$, TR is the repetition time and +inf is the plus infinity.

Cancer treatment study

For therapy studies, BALB/c mice were subcutaneously inoculated with 1 × 10⁶ 4T1 tumour cells on the right flank; C57BL/6 mice were subcutaneously inoculated with 1 × 10⁶ MC-38 tumour cells on the right flank. After the tumour size reached around 30–40 mm³, mice were randomly grouped ($n = 5$ per group). Mice from different groups were scanned individually by MRI using a T₁ mapping sequence and multi-slice T₁-weighted MRI sequence (pre-contrast MRI). The T-Fulips or Iso-Fulips were then injected intravenously with the injection dose of 10 mg per kilogram mouse body weight. At 24 h after the injection of contrast agents, the post-contrast MRI were acquired using the same T₁ mapping sequence and multi-slice T₁-weighted sequence as for pre-contrast MRI. The tumour size and body weight were recorded every two days after each treatment until 32 days post-irradiation, and the tumour volumes were calculated. The survival rate was recorded for up to 52 days post-irradiation.

Statistical analysis

All the quantitative data were expressed as mean ± s.d. and analysed with Microsoft Excel (2016), SPSS Statistics 26.0 software and GraphPad Prism (v.9.0). Comparisons of multiple groups at a single point were performed by using a one-way ANOVA with post-hoc analysis and two-sided Student's *t*-test. Survival data were analysed using a log-rank test. The Pearson's correlation coefficient *R* was used to calculate the

strength of a linear association between two variables. GraphPad Prism (v.9.0), FlowJo (v.10.6.2) and ImageJ (v.1.8.0) were used for statistical analysis and figure production. The statistical significance is indicated as NS (no significance), * $P < 0.05$, ** $P < 0.01$ and *** $P < 0.001$, 95% confidence level.

Reporting summary

Further information on research design is available in the Nature Portfolio Reporting Summary linked to this article.

Data availability

The main data that support the findings of this study are available within the Article, Supplementary Information and Supplementary Data 1. Other relevant data during the study are available for research purposes from the corresponding authors upon reasonable request. Source data are provided with this paper.

References

50. Csiszár, A. et al. Novel fusogenic liposomes for fluorescent cell labeling and membrane modification. *Bioconjug. Chem.* **21**, 537–543 (2010).

Acknowledgements

This work was supported by the National Natural Science Foundation of China (grant no. 82272136, Z.Z.; no. 31971302, W.G.), the Special Project from the National Science and Technology Program for Central Guided Local Development (grant no. 2021L3010075, Z.Z.), the Start-up Programme from Xiamen University (Z.Z.), the project funded by China Postdoctoral Science Foundation (grant no. 2022M722654, C.S.), the National University of Singapore Start-up Grant (NUHSRO/2020/133/Startup/08, X.C.), National University of Singapore School of Medicine Nanomedicine Translational Research Program (NUHSRO/2021/034/TRP/09/Nanomedicine, X.C.)

and National Medical Research Council Centre Grant Programme (CG21APR1005, X.C.). We cordially thank G. Liu and C. Liu for fruitful discussions, Z. Huang for her support in MRI scanning and D. Guo and X. Zhang from the School of Public Health at Xiamen University for their support in using the microscope and flow cytometer.

Author contributions

Z.Z., C.S., W.G. and X.C. conceived and designed the project. C.S., F.Z., C.D., Q.Z. and H.Y. performed the material synthesis and characterizations. C.S. and Q.Z. prepared the samples. C.S. and Q.Z. acquired and analysed all the MRI data. C.S., Q.Z., Y.Y., Xinyi Zhang, S.N., F.Z., C.D. and H.C. performed the animal study. X.W., Z.G., Xianzhong Zhang and J.G. analysed and discussed the results. C.S., Z.Z., W.G. and X.C. analysed the results and cowrote the paper. All the authors discussed and approved the final version.

Competing interests

The authors declare no competing interests.

Additional information

Supplementary information The online version contains supplementary material available at <https://doi.org/10.1038/s41565-022-01261-7>.

Correspondence and requests for materials should be addressed to Weisheng Guo, Xiaoyuan Chen or Zijian Zhou.

Peer review information *Nature Nanotechnology* thanks Roger Geiger, Jeff Bulte and the other, anonymous, reviewer(s) for their contribution to the peer review of this work.

Reprints and permissions information is available at www.nature.com/reprints.

Reporting Summary

Nature Portfolio wishes to improve the reproducibility of the work that we publish. This form provides structure for consistency and transparency in reporting. For further information on Nature Portfolio policies, see our [Editorial Policies](#) and the [Editorial Policy Checklist](#).

Statistics

For all statistical analyses, confirm that the following items are present in the figure legend, table legend, main text, or Methods section.

n/a Confirmed

- The exact sample size (n) for each experimental group/condition, given as a discrete number and unit of measurement
- A statement on whether measurements were taken from distinct samples or whether the same sample was measured repeatedly
- The statistical test(s) used AND whether they are one- or two-sided
Only common tests should be described solely by name; describe more complex techniques in the Methods section.
- A description of all covariates tested
- A description of any assumptions or corrections, such as tests of normality and adjustment for multiple comparisons
- A full description of the statistical parameters including central tendency (e.g. means) or other basic estimates (e.g. regression coefficient) AND variation (e.g. standard deviation) or associated estimates of uncertainty (e.g. confidence intervals)
- For null hypothesis testing, the test statistic (e.g. F , t , r) with confidence intervals, effect sizes, degrees of freedom and P value noted
Give P values as exact values whenever suitable.
- For Bayesian analysis, information on the choice of priors and Markov chain Monte Carlo settings
- For hierarchical and complex designs, identification of the appropriate level for tests and full reporting of outcomes
- Estimates of effect sizes (e.g. Cohen's d , Pearson's r), indicating how they were calculated

Our web collection on [statistics for biologists](#) contains articles on many of the points above.

Software and code

Policy information about [availability of computer code](#)

Data collection

Transmission electron microscopy (TEM) images were acquired on a TecnaiG2 Spirit equipment with a voltage at 120 kV. Dynamic light scattering measurements were performed at a SZ-100 nano particle analyzer (HORIBA Scientific). Proton nuclear magnetic resonance (1H NMR) spectra were recorded on a Bruker AVANCE-III scanner. Flow cytometry data were collected using Cytotflex LX and the equipped software (CytExpert). Radical spectra were recorded on a Bruker electron paramagnetic resonance (EPR) spectroscopy (Bruker EMX-10/12). Tissue and tumor samples for immunofluorescent staining were observed using Zeiss LSM 880+Airyscan. Biodistribution measurements were performed on Carestream Imaging Station system. Magnetic resonance imaging (MRI) measurements were performed on a 9.4T small animal scanner (Bruker 94/20, Germany) equipped with small animal specific body coil.

Data analysis

All the quantitative data were expressed as mean \pm s.d. and analyzed with SPSS statistics 26.0 software. GraphPad Prism (v.9.0), FlowJo (v10.6.2), CytExpert (2.3) and Image J (v1.8.0) were used for statistical analysis and figure production. MRI data analysis and processing: The MRI maps were obtained by fitting weighted images into relation parameters assuming single exponential decay. The procedure was conducted on the built-in software (Paravision 5.1, Bruker). The relaxation time was further analyzed by Image J. Pearson's correlation analysis: <https://www.socscistatistics.com/tests/pearson/>.

For manuscripts utilizing custom algorithms or software that are central to the research but not yet described in published literature, software must be made available to editors and reviewers. We strongly encourage code deposition in a community repository (e.g. GitHub). See the Nature Portfolio [guidelines for submitting code & software](#) for further information.

Data

Policy information about [availability of data](#)

All manuscripts must include a [data availability statement](#). This statement should provide the following information, where applicable:

- Accession codes, unique identifiers, or web links for publicly available datasets
- A description of any restrictions on data availability
- For clinical datasets or third party data, please ensure that the statement adheres to our [policy](#)

The source data underlying Figure 2, Figure 3, Figure 4, Figure 5, Figure 6, and western blot are provided with this paper. The main data that support the findings of this study are available within the article, source data and its Supplementary Information. Other relevant data during the study are available for research purposes from the corresponding authors upon reasonable request.

Field-specific reporting

Please select the one below that is the best fit for your research. If you are not sure, read the appropriate sections before making your selection.

- Life sciences Behavioural & social sciences Ecological, evolutionary & environmental sciences

For a reference copy of the document with all sections, see [nature.com/documents/nr-reporting-summary-flat.pdf](https://www.nature.com/documents/nr-reporting-summary-flat.pdf)

Life sciences study design

All studies must disclose on these points even when the disclosure is negative.

Sample size	No statistical method was used to predetermine the sample size for each study. For property measurement experiments, samples were prepared and tested at least twice. For in vivo studies, each group contains at least 3 ($n \geq 3$) for evaluating the statistical significance. A precise value of 'n' were provided in the legends of figures. Sample size was chosen to ensure reproducibility of the experiments in accordance with the replacement, reduction and refinement principles of animal ethics regulation.
Data exclusions	No data was excluded from the analysis.
Replication	For property measurement experiments, samples were replicated and tested independently for 2-3 times and after analysis the standard deviation was displayed. For each experiment the statistical analysis is indicated in the figure legends.
Randomization	Randomization was used to divide up the animals for in vivo treatment study.
Blinding	No blinding was employed as the researcher performing the treatment was also responsible for the analysis. The researchers should keep careful track of protocols because that most of the experiments needed multiple treatments (including formulation, cells or mouse tumor treatment, sample collection, and so on). Hence, it would be difficult to blind the investigators to group allocation during data collection and analysis.

Reporting for specific materials, systems and methods

We require information from authors about some types of materials, experimental systems and methods used in many studies. Here, indicate whether each material, system or method listed is relevant to your study. If you are not sure if a list item applies to your research, read the appropriate section before selecting a response.

Materials & experimental systems

n/a	Involved in the study
<input type="checkbox"/>	<input checked="" type="checkbox"/> Antibodies
<input type="checkbox"/>	<input checked="" type="checkbox"/> Eukaryotic cell lines
<input checked="" type="checkbox"/>	<input type="checkbox"/> Palaeontology and archaeology
<input type="checkbox"/>	<input checked="" type="checkbox"/> Animals and other organisms
<input checked="" type="checkbox"/>	<input type="checkbox"/> Human research participants
<input checked="" type="checkbox"/>	<input type="checkbox"/> Clinical data
<input checked="" type="checkbox"/>	<input type="checkbox"/> Dual use research of concern

Methods

n/a	Involved in the study
<input checked="" type="checkbox"/>	<input type="checkbox"/> ChIP-seq
<input type="checkbox"/>	<input checked="" type="checkbox"/> Flow cytometry
<input checked="" type="checkbox"/>	<input type="checkbox"/> MRI-based neuroimaging

Antibodies

Antibodies used	<p>Anti-Thioredoxin antibody (rabbit monoclonal, abcam, cat#: ab273877, clone: EPR23843-48), dilution 1:200; Anti-TXNIP antibody (mouse monoclonal, abcam, cat#: 3700T, clone: EPR14774), dilution 1:200; β-Actin Mouse mAb (CST, cat#: 3700T, clone: 8H10D10), dilution 1:1000; HRP-conjugated goat anti-rabbit IgG (Sangon Biotech, cat#: D110058), dilution 1:10000; HRP-conjugated goat anti-mouse IgG (Sangon Biotech, cat#: D110087), dilution 1:10000; Pacific Blue anti-mouse F4/80 (Biolegend, cat#: 123123, clone: BM8), dilution 1:200; FITC anti-mouse/human CD11b (Biolegend, cat#: 101206, clone: M1/70), dilution 1:200; FITC anti-mouse CD3 (Biolegend, cat#: 100204, clone: 17A2), dilution 1:200; PE anti-mouse CD4 (Biolegend, cat#: 100408, clone: GK1.5), dilution 1:200; PE anti-mouse CD8a (Biolegend, cat#: 100708, clone: 53-6.7), dilution 1:200; Alexa Fluor 488 anti-mouse FOXP3 (Biolegend, cat#: 126405, clone: MF-14), dilution 1:200; APC anti-mouse IFN-γ (Biolegend, cat#: 505809, clone: XMG1.2), dilution 1:200; PE/Cyanine7 anti-mouse IFN-γ (Biolegend, cat#: 505825, clone: XMG1.2), dilution 1:200; Pacific Blue anti-mouse CD45 (Biolegend, cat#: 103126, clone: 30-F11), dilution 1:200; APC anti-mouse Ly-6G/Ly-6C (Gr-1) (Biolegend, cat#: 108412, clone: RB6-8C5), dilution 1:200; APC anti-mouse H-2Kb bound SIINFEKL (Biolegend, cat#: 144606, clone: 25-D1.16), dilution 1:200; Anti-mouse CD3ϵ-(Fab')₂ fragments (BioXCell, cat#: BE0001, clone: 145-2C11); Anti-mouse IgG-(Fab')₂ fragments (BioXCell, cat#: BE0091);</p>
Validation	<p>The antibodies listed above are standard reagents used in the field and validated in the literature as cited on the manufacturers websites, as well as by the manufacturers data sheets themselves.</p> <ol style="list-style-type: none"> 1. Anti-Thioredoxin antibody: https://www.abcam.cn/thioredoxin--trx-antibody-epr23843-48-ab273877.html 2. Anti-TXNIP antibody: https://www.abcam.com/txnip-antibody-epr14774-chimeric-ab210826.html 3. β-Actin Mouse mAb: https://www.cellsignal.com/products/primary-antibodies/b-actin-8h10d10-mouse-mab/3700 4. HRP-conjugated goat anti-rabbit IgG: https://www.sangon.com/productDetail?productInfo.code=D110058 5. HRP-conjugated goat anti-rabbit IgG: https://www.sangon.com/productDetail?productInfo.code=D110087 6. Pacific Blue anti-mouse F4/80: https://www.biolegend.com/en-us/products/pacific-blue-anti-mouse-f4-80-antibody-4075?GroupID=BLG5319 7. FITC anti-mouse/human CD11b: https://www.biolegend.com/en-us/products/fitc-anti-mouse-human-cd11b-antibody-347?GroupID=BLG10660 8. FITC anti-mouse CD3: https://www.biolegend.com/en-us/products/fitc-anti-mouse-cd3-antibody-45?GroupID=BLG6732 9. PE anti-mouse CD4: https://www.biolegend.com/en-us/products/pe-anti-mouse-cd4-antibody-250?GroupID=BLG4745 10. PE anti-mouse CD8a: https://www.biolegend.com/en-us/products/pe-anti-mouse-cd8a-antibody-155?GroupID=BLG2559 11. Alexa Fluor 488 anti-mouse FOXP3: https://www.biolegend.com/en-us/products/alexa-fluor-488-anti-mouse-foxp3-antibody-4661?GroupID=BLG5706 12. APC anti-mouse IFN-γ: https://www.biolegend.com/en-us/products/apc-anti-mouse-ifn-gamma-antibody-993?GroupID=GROUP24 13. PE/Cyanine7 anti-mouse IFN-γ: https://www.biolegend.com/en-us/products/pe-cyanine7-anti-mouse-ifn-gamma-antibody-5865?GroupID=GROUP24 14. Pacific Blue anti-mouse CD45: https://www.biolegend.com/en-us/products/pacific-blue-anti-mouse-cd45-antibody-3102?GroupID=BLG6841 15. APC anti-mouse Ly-6G/Ly-6C (Gr-1): https://www.biolegend.com/en-us/products/apc-anti-mouse-ly-6g-ly-6c-gr-1-antibody-456?GroupID=BLG4876 16. APC anti-mouse H-2Kb bound SIINFEKL: https://www.biolegend.com/en-us/products/apc-anti-mouse-h-2kb-bound-to-siinfekl-antibody-7882?GroupID=BLG9387 17. Anti-mouse CD3ϵ-(Fab')₂ fragments: https://bxc.com/product/m-cd3e-fab2-fragments/ 18. Anti-mouse IgG-(Fab')₂ fragments: https://bxc.com/product/hamster-fab2-fragments/

Eukaryotic cell lines

Policy information about [cell lines](#)

Cell line source(s)	4T1, MC38 cell lines were purchased from American Type Culture Collection (ATCC). B16F10-OVA are from Cell Bank of Shanghai, Chinese Academy of Sciences (Shanghai, China)
Authentication	Cell lines have been authenticated by short tandem repeat profiling, and the results were compared with reference database.
Mycoplasma contamination	All cell lines tested negative for mycoplasma contamination.
Commonly misidentified lines (See ICLAC register)	No commonly misidentified cell lines were used.

Animals and other organisms

Policy information about [studies involving animals](#); [ARRIVE guidelines](#) recommended for reporting animal research

Laboratory animals	Six- to eight-week-old female BALB/c and C57BL/6 mice and were purchased from Beijing Vital River Laboratory Animal Technology Co. Ltd. (Beijing, China). OT-I mice were approved purchased from Laboratory Animals Center for Guangzhou Medical University. Animals were housed in groups of 4–5 mice per cage, maintained at a temperature of ~25 °C in a humidity-controlled environment with a 12 h light/dark cycle.
--------------------	---

Wild animals	This study did not involve wild animals.
Field-collected samples	This study did not involve sample collected from the field.
Ethics oversight	All animal experiments were carried out in accordance with the Guide Protocol of Laboratory Animals, approved by the Ethics Committee of the Xiamen University and Guangzhou Medical University.

Note that full information on the approval of the study protocol must also be provided in the manuscript.

Flow Cytometry

Plots

Confirm that:

- The axis labels state the marker and fluorochrome used (e.g. CD4-FITC).
- The axis scales are clearly visible. Include numbers along axes only for bottom left plot of group (a 'group' is an analysis of identical markers).
- All plots are contour plots with outliers or pseudocolor plots.
- A numerical value for number of cells or percentage (with statistics) is provided.

Methodology

Sample preparation	Tissue was collected and incubated in a digestion cocktail containing collagenase IV (100 U/mL, Sigma-Aldrich), DNase I (20 µg/mL, Sigma-Aldrich) in complete RPMI at 37 °C for 60 min. Tissue was then filtered through a 70-µm filter. Cells were mixed in 4 ml of Percoll solution and centrifuged at 800g for 15 min without a brake. The Percoll layer was removed and cells were diluted in 5 ml of 2% fetal bovine serum (FBS). Cells were treated with ACK buffer and resuspended in 1% BSA. At this point, cells were counted using an automated cell counter (Thermo Fisher Scientific). For tumor tissues, the antibody staining solution was added to each cell samples at a concentration of about 1*10e6 and stained for 30 min at 4 °C before running the flow cytometry tests. For isolating T cells, the cells were cultured and stained following the instruction of the Mouse T Cell Isolation Kit provided by the product company (BioLegend).
Instrument	Flow cytometry data were collected using Cytotflex LX and the equipped CytExpert (2.3) software.
Software	Flow cytometry data were analyzed using FlowJo (v10.6.2) for windows.
Cell population abundance	The purity of post-sort fractions is regularly measured by the software. The fractions were around 70-90%.
Gating strategy	A forward-scatter/side-scatter gate was used to gate on lymphocytes to exclude debris. All gating strategies were provided in the supplementary figures.

Tick this box to confirm that a figure exemplifying the gating strategy is provided in the Supplementary Information.